Wind-Wave Attenuation in Arctic Sea Ice: A Discussion of Remote Sensing Capabilities

Fabrice Collard, Louis Marié, Frédéric Nouguier, Marcel Kleinherenbrink, Frithjof Ehlers, Fabrice Ardhuin

JGR Oceans

RESEARCH ARTICLE
10.1029/2022JC018654

Special Section:
The Arctic: An AGU Joint Special Collection

Wind-Wave Attenuation in Arctic Sea Ice: A Discussion of Remote Sensing Capabilities

Fabrice Collard[1], Louis Marié[2], Frédéric Nouguier[2], Marcel Kleinherenbrink[3], Frithjof Ehlers[3], and Fabrice Ardhuin[2]

[1]OceanDataLab, Locmaria-Plouzané, France, [2]Univ. Brest, CNRS, Ifremer, IRD, Laboratoire d'Océanographie Physique et Spatiale, Brest, France, [3]TU Delft, Delft, The Netherlands

Key Points:

- Wave patterns in sea ice can be found in radar and optical remote sensing data
- We provide a quantitative estimation of wave height, wavelength and direction from ICESat-2 and Sentinel-2 data
- Wavelengths and directions in full-focus SAR altimetry and CFOSAT SWIM are consistent with other sensors

Correspondence to:
F. Ardhuin,
ardhuin@ifremer.fr

Citation:
Collard, F., Marié, L., Nouguier, F., Kleinherenbrink, M., Ehlers, F., & Ardhuin, F. (2022). Wind-wave attenuation in Arctic sea ice: A discussion of remote sensing capabilities. *Journal of Geophysical Research: Oceans*, *127*, e2022JC018654. https://doi.org/10.1029/2022JC018654

Received 20 MAR 2022
Accepted 6 JUN 2022

Abstract Wind-generated waves strongly interact with sea ice and impact air-sea exchanges, operations at sea, and marine life. Unfortunately, the dissipation of wave energy is not well quantified and its possible effect on upper ocean mixing and ice drift is still mysterious. As the Arctic is opening up and wave energy increases, the limited amount of *in situ* observations is a clear limitation to our scientific understanding. Both radar and optical remote sensing has revealed the frequent presence of waves in ice, and could be used more systematically to investigate wave-ice interactions. Here we show that, in cloud-free conditions, Sentinel-2 images exhibit brightness modulations in ice-covered water, consistent with the presence of waves measured a few hours later by the ICESat-2 laser altimeter. We show that a full-focus SAR processing of Sentinel-3 radar altimeter data also reveals the presence and wavelengths of waves in sea ice, within minutes of Sentinel-2 imagery. The SWIM instrument on CFOSAT is another source of quantitative evidence for the direction and wavelengths of waves in ice, when ice conditions are spatially homogeneous. In the presence of sea ice, a quantitative wave height measurement method is not yet available for all-weather near-nadir radar instruments such as altimeters and SWIM. However, their systematic colocation with optical instruments on Sentinel-2 and ICESat-2, which are less frequently able to observe waves in sea ice, may provide the empirical transfer functions needed to interpret and calibrate the radar data, greatly expanding the available data on wave-ice interactions.

Plain Language Summary Waves generated by winds over the ocean propagate in ice-covered regions where they can be strongly attenuated and can contribute to breaking up the ice and pushing the ice around. Wavy patterns are clearly visible in remote sensing data collected by different instruments including the ICESat-2 laser altimeter, Sentinel-1 imaging radar, the Sentinel-2 optical imager, Sentinel-3 radar altimeter, and CFOSAT wave-measuring instrument SWIM. Here, we show examples of such patterns and propose a quantitative interpretation of ICESat-2 and Sentinel-2 that is consistent with waves generated by storms in the Barents Sea that are observed to travel under the ice over hundreds of kilometers. For Sentinel-3 and SWIM, a quantification of wave heights will have to be validated, possibly based on data from the other two instruments. This may strongly expand the quantity of available information for scientific investigations and operational applications.

1. Introduction

The evolving ice cover in the Arctic is becoming more exposed to wind-generated waves that now develop over larger open water regions and grow to larger heights and wavelengths (Stopa et al., 2016; Thomson & Rogers, 2014). When these waves reach the ice edge, they are strongly attenuated by sea ice but the components of the sea state with the longest periods may still break up the ice far from the ice edge, over hundreds of kilometers (Collins et al., 2015). Wave attenuation contributes to ice drift (Thomson, Lund, et al., 2021), under-ice mixing, ice formation (Sutherland & Dumont, 2018), or melting (Horvat & Tziperman, 2017). Whereas numerical wave models have made considerable progress in ice-free waters, the forecasting of wave conditions in ice-covered regions is limited by a poor knowledge of wave attenuation. The investigation of wave-ice interactions has been the topic of a growing number of field experiments (Squire, 2020; Wadhams et al., 1986). Many of these experiments have focused near the ice edge where access from ships is possible (Doble et al., 2011; Thomson et al., 2018) and where the attenuation is strongest. However, the spatial heterogeneity of the ice field and the generally low values of wave heights makes the measurement analysis difficult and prone to contamination by noise (Thomson, Hoseková, et al., 2021). Still, *in situ* experiments have been critical in identifying ice type as an

important factor in wave attenuation (Rogers et al., 2016), and ruling out wave scattering as the dominant mechanism of wave attenuation (Ardhuin et al., 2016). Remote sensing from airplanes or satellites can provide unique measurements of waves, far into the ice field, giving maps of surface elevation (Sutherland & Gascard, 2016) or vertical orbital velocities (Ardhuin et al., 2015) that provide a quantitative estimate of local wave heights, wavelengths, and directions.

Using the most extensive waves-in-ice data set to date, provided by the Sentinel-1 wave mode, a wide range of attenuation rates was found for waves entering sea ice from the ice-free ocean (Stopa, Sutherland, & Ardhuin, 2018). These different attenuations are probably caused by different ice properties, in particular ice thickness and floe sizes. Ardhuin et al. (2020) confirmed the importance of floe size, with a much stronger attenuation for floe sizes much larger than the wind-wave wavelength. These analyses have been performed in the Southern Ocean where 5 m resolution Synthetic Aperture Radar (SAR) imagery is routinely collected with the Wave Mode of Sentinel-1 (Hasselmann et al., 2012).

The main limitation of these high-quality wave-mode SAR images is their sparse acquisition: one can only guess what kind of waves and ice are present between two images that are 20 km by 20 km across but separated by 100 km. The coarser 10 m resolution Interferometric Wide swath mode (IW) is more seldom used over sea ice but provides continuous images that allow following waves 500 km or more into the sea ice (Stopa, Ardhuin, et al., 2018). Even coarser images, with an azimuth resolution of 43 m, are most often acquired by Sentinel-1 over the Arctic, using the Extended Wide Swath mode (EW), which is prioritized to get the widest coverage of sea ice. Because only waves with wavelengths larger than about 4 SAR pixels can be resolved, the EW mode can detect only swells with relatively large wavelengths. In practice SAR measurements of waves in sea ice can be very accurate with a sharp contrast for wave heights larger than 50 cm in wave-mode and IW mode Sentinel 1 data (Ardhuin et al., 2017), which is sufficient to measure the strong attenuations near the ice edges. For smaller wave heights, it can be difficult to separate the wave signature from the signatures of ice heterogeneities, in particular in the presence of leads where ice is not broken up by the wave field.

The recent analysis of ICESat-2 laser altimeter data by Horvat et al. (2020) shows that there are ice-height variations induced by ocean waves in many satellite passes, which may provide an interesting source of cross-validation of both techniques for studying waves in ice. While looking for different sources of data to help in the interpretation of ICESat-2 data we also found wave patterns in Sentinel-2 optical imagery, and Sentinel-3 Synthetic Aperture Radar Altimeter reprocessed with Full-Focus SAR (FF-SAR) as described by Kleinherenbrink et al. (2020) and Altiparmaki et al. (2022). These different remote sensing techniques are influenced by waves in different ways, be it the change in surface elevation, slope, or line-of-sight velocity, as summarized in Figure 1.

The goal of the present paper is to discuss the complementarity of data from SAR, ICESat-2, and other satellite instruments for the detection and measurement of wave properties in sea ice, in particular across the ice edge where waves-ice interactions are expected to be strongest. We have thus looked at two cases, one on 23 March 2019 to the East of Spitzbergen, taken from Horvat et al. (2020) for which Sentinel-1 and Sentinel-2 data are also available. The second case is in the same region, on 12 March 2021, and is also covered by Sentinel-3 and th Chn-a-Franc Ocan SatllCFOSAT. Discussions and conclusions follow in Section 4.

2. Case of 23 March 2019

As illustrated in Figure 2, a storm swept through the Barents Sea, from the West, on March 22, with a band of high winds exceeding 20 m/s from Spitzbergen to Norway, dying out after 19:00 UTC according to the ECMWF operational analyses and forecasts that we also use in our wave model. These high winds generated swells with wave heights exceeding 6 m that persisted until March 23 at 14:00 UTC.

Wave properties were estimated using a configuration of the WAVEWATCH III model (The WAVEWATCH III® Development Group, 2019) that uses a 12 km resolution polar stereographic grid. Forcing uses winds from ECMWF operational forecasts and analyses, and sea ice concentration from the Ifremer product derived from the SSM/I satellite radiometer. For the ice thickness we have used a simple constant thickness h_i with $0.25 \leq h_i \leq 1.0$ m to give a plausible range of wave attenuation that is broadly consistent with thin ice estimations from remote sensing data (Kaleschke et al., 2012). The parameterizations of wave-ice interactions and ice break-up are adapted from Boutin et al. (2018) with the parameter settings adjusted by Ardhuin et al. (2020).

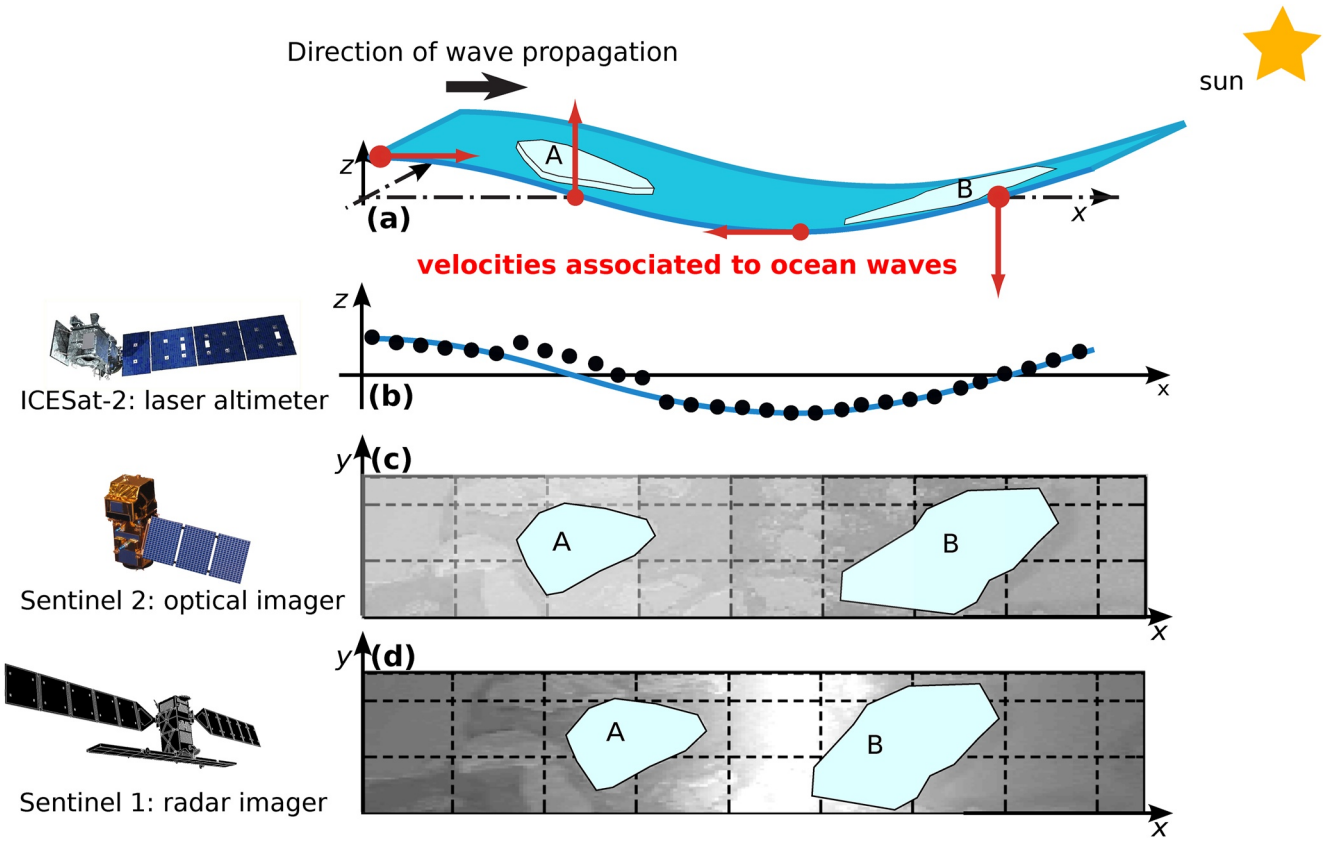

Figure 1. How different remote sensing techniques detect or measure waves in the presence of sea ice? (b) We expect that waves introduce vertical displacement, which change the range-measurements of ICESat-2 laser altimeter, which includes the water level and ice freeboard (Sutherland & Gascard, 2016), (c) introduce a surface brightness variation, possibly due to the sloping surface as discussed in Section 2.2, and picked up by optical imagers if the sun is low enough over the horizon, and (d) the vertical velocities of the ice produce a constructive velocity bunching effect in SAR imagery (Ardhuin et al., 2017; Lyzenga et al., 1985).

2.1. Quantitative Information on Waves in Ice From ICESat-2

Horvat et al. (2020) reported the detection of waves in sea ice on 23 March 2019, along the track of ICESat-2 shown in Figure 3. ICESat-2 beams have a 13 m diameter footprint and are thus capable of sampling relatively short waves. Here, we use the same data set, namely Level-3a ATL07 ice elevation (Kwok et al., 2021), with a pass near 4:00 UTC. Due to cloud cover, ice elevation is not available all the way to the ice edge but starts around 77.6°N. It is often the case that on-ice winds tend to blow the cloud cover from the relatively warm open water over the ice.

Beyond the presence of waves in sea ice that gives characteristic ice elevation profiles, with examples shown in Figure 3e–3g, it would be interesting to quantify wave heights, periods, and directions. ICESat-2 ice elevation data are provided for 6 beams arranged in 3 pairs, with a 90 m separation within each pair and a separation of the different pairs by about 3.3 km. As a result, the ice elevation samples only very few waves, in particular when the angle between the satellite track and wave propagation direction gets close to 90°. As a result there is a large uncertainty on the wave height, which may be estimated as 4 times the standard deviation of ice elevation. Here we find 1.5, 1.1, and 0.4 m for the 3 segments shown in Figure 3. The evolution of wave height along the ICESat-2 track is compared in Figure 4 to the two model simulations with ice thicknesses of 0.25 and 1 m.

Besides wave heights, the clear coherence within pairs of beams makes it possible to estimate mean wave direction (Yu et al., 2021). Because the sea ice prevents the formation of a local wind-sea and strongly dissipates swells propagating over longer distances, the wave spectrum is generally narrow in directions (Ardhuin et al., 2016). Assuming that the directional wave spectrum is narrow, for any band of latitude of the order of 0.1° (about 12 km along-track), we estimated the latitudinal shift dy that maximizes the correlation between the ice elevations measured by two beams in a pair. As we know the track separation in longitude dx, the ratio $-dy/dx$ is the tangent of the

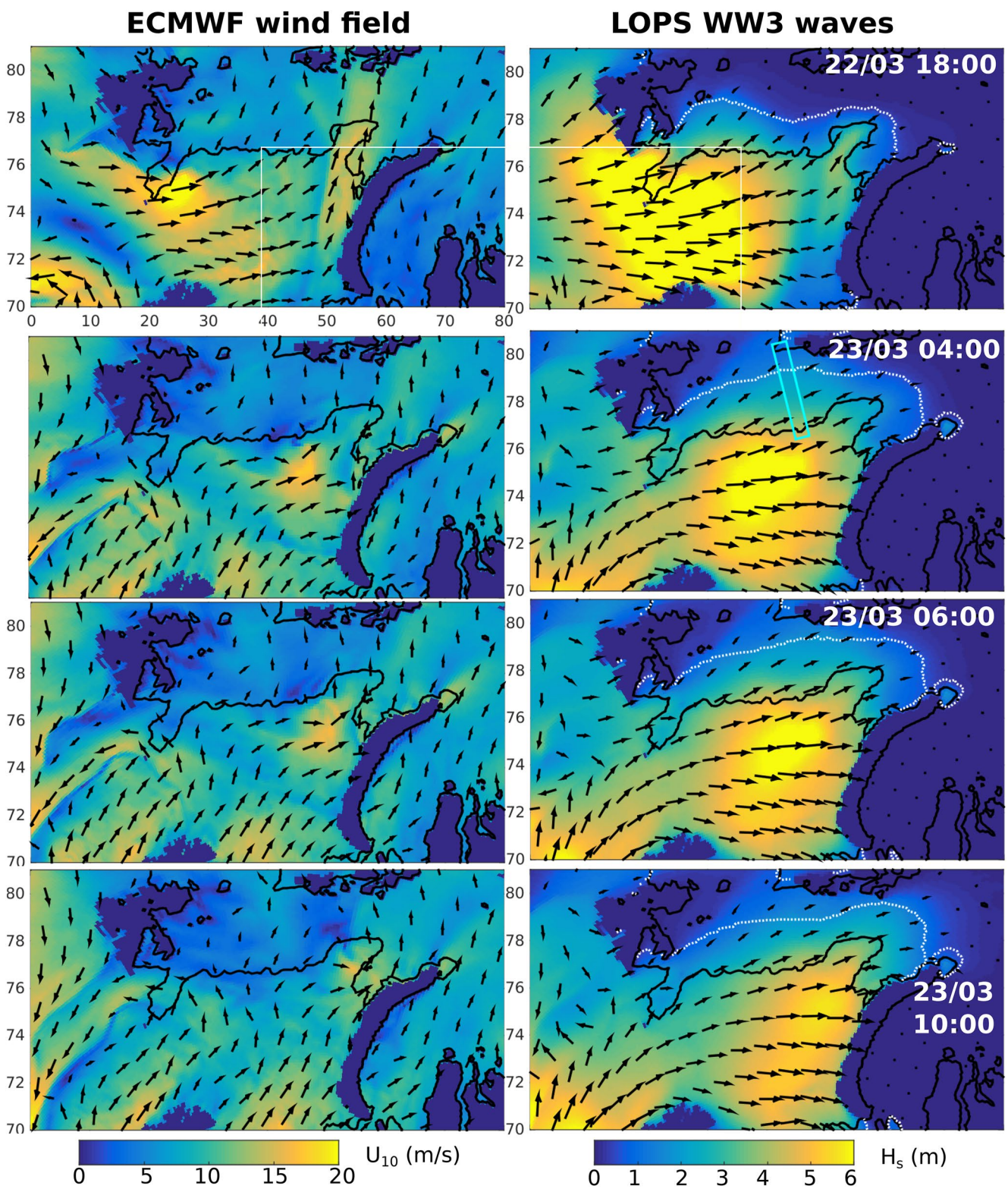

Figure 2. Wind and wave conditions from 18:00 UTC on 22 March 2019 (top panels) to 10:00 UTC on 23 March (bottom panels). In each panel the black line marks the location of the ice edge. Wind speed and directions are given by ECMWF IFS Operational analyses and forecasts, and waves are given by our wave model, here using an ice thickness $h_i = 0.25$ m. The wave model also predicts ice break-up, with the 200 m contour of floe diameter shown with the dotted white line. The cyan rectangle on the second line is the transect in which model data was compared to ICESat-2 data.

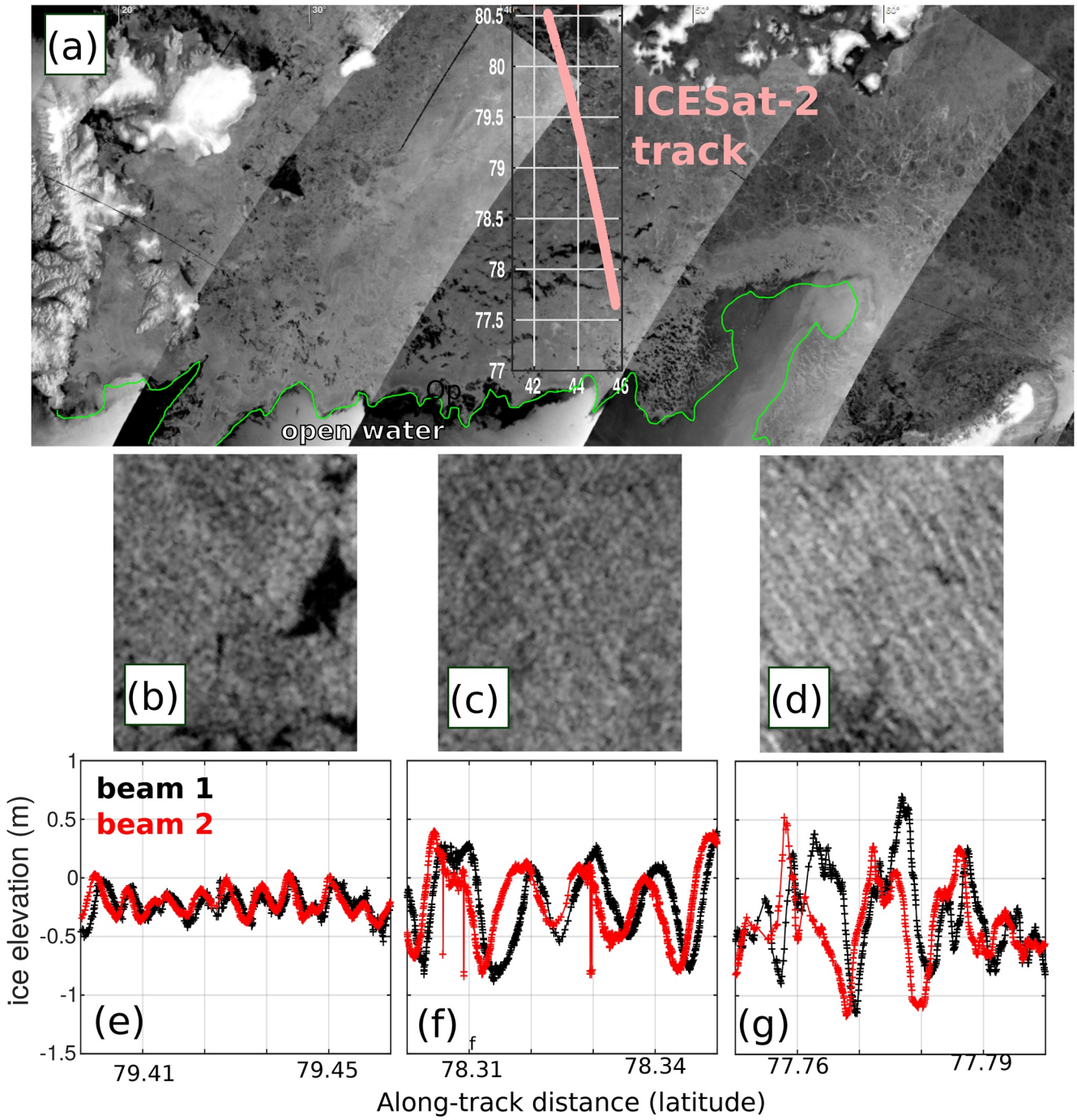

Figure 3. Wave signatures in Sentinel-1 and ICESat-2 on 23 March 2019. (a) The portion of ICESat-2 track where wave signals are detected in the Level3a ATL07 ice elevation product is show in pink, overlaid on the mosaic of Sentinel-1 Extended Wide Swath mode (EW) intensity. Svalbard is to the left and Novaya Zemlya to the bottom right. The ice edge is the green line. (b–d) are pieces of the Sentinel one images, each extending 0.05° in latitude, along the ICESat-2 tracks, with surface elevations shown in the bottom panels (e–g). Ice elevations are only shown for the first pair of ICESat-2 beams.

iso-phase patterns in the elevation data, which we take to be aligned with the wave crests. These mean directions are shown in Figure 4, where the squared correlation coefficients are above 0.8. The general trend is that wave directions veer from a west-south-westerly directions of 240–250 near the ice edge, to a more southerly direction around 225° as they approach 80°N. This is consistent with the general result that the mean wave direction tends to turn toward the direction that gives the shortest distance to the ice edge, because wave attenuation is lower

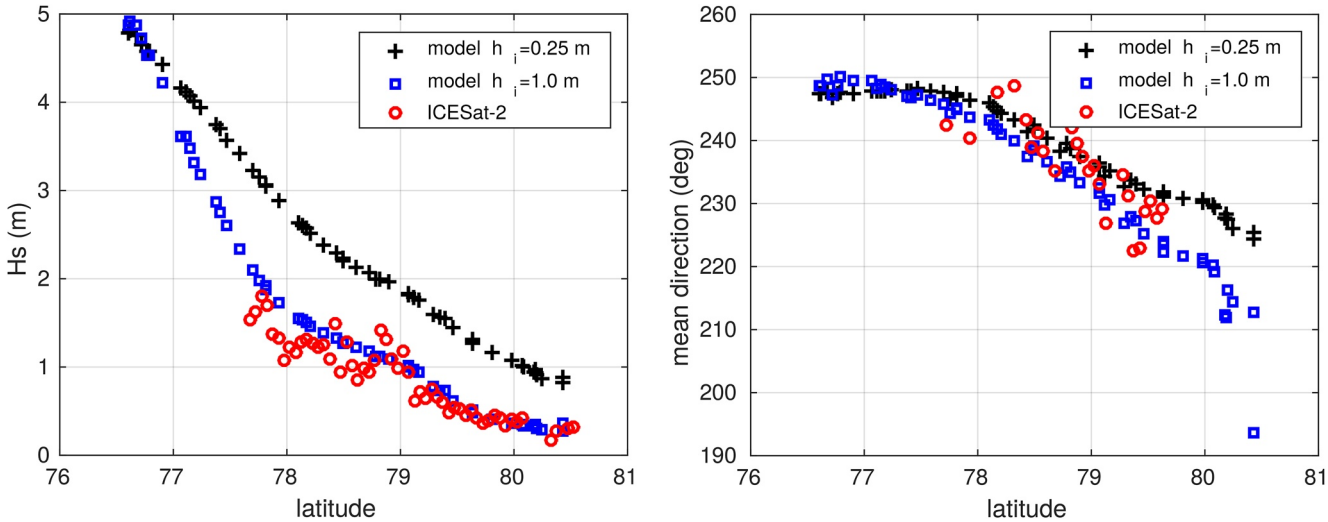

Figure 4. Wave heights and mean wave directions (from, nautical convention) along the ICESat-2 track at 4:00 UTC on 23 March 2019, according to two different model simulations or taken as the average of the 6 wave heights estimated for each of the six ICESat-2 laser beams.

for shorter propagation distances across the ice. This is also why the model with the stronger dissipation has a different mean direction as waves get farther into the ice.

Once the direction is known, we may convert the apparent along-track wavenumber k_a that is the projection of the actual wavenumbers on the satellite track, into the actual wavenumber k,

$$k = k_a / \cos(\theta_w - \theta_t). \quad (1)$$

Using these wavenumbers k, the main difficulty in defining a mean wavelength, that can be compared to the modeled mean period, is that the ice elevation contains also large-scale variations in freeboard between ice and water. These freeboard variations contribute to the ice height at long wavelengths. In our case, this effect gives a positive bias for the mean wavelength for latitudes under 78° (not shown). Further in the ice, the elevation spectrum appears to have lower variance at low frequencies and gives a mean wavelength around 310 m that is consistent with the modeled mean period of 15 s, using the Airy wave dispersion relation that is applicable for these long waves and thin ice conditions. Alternatively, one may use a peak wavelength to avoid contamination by large-scale freeboard variations.

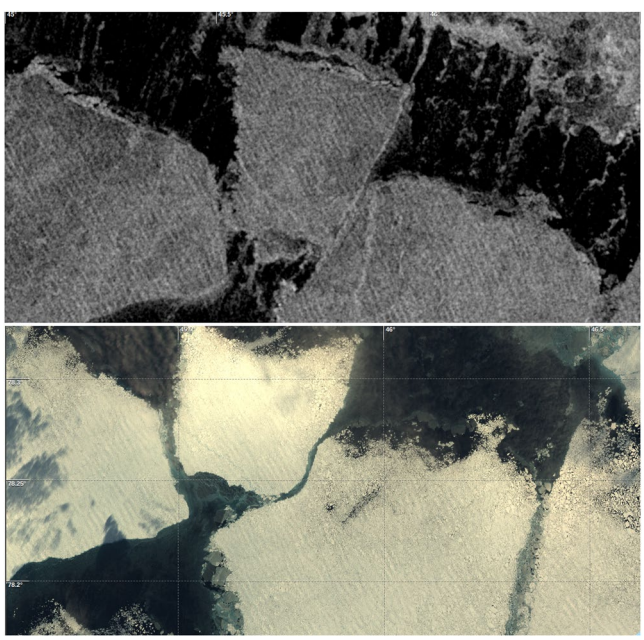

Figure 5. Same ice floes observed by Sentinel 1 at 9:00 UTC and Sentinel 2 at 11:07 UTC on 23 March 2019, around 78.15°N, 46.00°E. The Sentinel two image is a true color composite using bands B02, B03, and B04.

For this same event, additional information is provided by Sentinel 2 with an image acquired at 11:07 UTC on the same day. The same ice floes and leads are clearly identifiable in both Sentinel-1 and Sentinel-2 imagery, as shown in Figure 5. The 10 m resolution of S2 imagery allows to see that what could look like a solid 8-km long floe is actually shattered in many floes with sizes under 50 m. These small floes have not yet moved much with respect to one another. Stripes in the image brightness clearly correspond to waves with a direction and wavelength that is very similar to what was found in the S1 image and in the ICESat-2 data.

2.2. Interpreting Wave Patterns in Sentinel-2 Two Imagery

The image intensity in optical imagery is generally a function of the sun and sensor orientation and the surface bidirectional reflectance distribution function. For the scene shown in Figure 5, the sun zenithal angle is $\theta_{\text{Sun}} = 79.4°$ (i.e., 10.6° above the horizon), with a sun azimuth of 215°, and the instrument zenith angle is around $\theta_d = 10.0°$. For observation zenith angles smaller

than 30°, snow on sea ice can be considered a Lambertian scatterer (Dirmhirn & Eaton, 1975). In this limit, the specific intensity leaving a horizontal snow-covered sea ice surface toward the detector, in azimuth ϕ_d and zenith angle θ_d, in W m^{-2} sr^{-1}, is given by

$$I(\theta_d, \phi_d) = \frac{1}{\pi} I_{\text{Sun}} \rho \cos(\theta_{\text{Sun}}),$$

where I_{Sun} is the Sun irradiance, in W m^{-2}, ρ is the (dimensionless) surface reflectance, and θ_{Sun} is the sun zenith angle. The effects of detector characteristics, Sun irradiance, and nominal Sun zenith angle are taken into account by the L1c processor, to yield the Top-Of-Atmosphere estimate of the reflectance ρ_{L1c}.

These corrections do not take into account the sloping of the ice surface as it is tilted by underlying waves. As a result, the sun zenith angle should be replaced by angle θ_l between the vector locally normal to the ice or snow surface and the vector pointing from the surface to the Sun, giving rise to modulations of the L1c TOA reflectance as

$$\rho_{\text{L1c}} = \rho_{\text{true}} \frac{\cos(\theta_l)}{\cos(\theta_{\text{Sun}})}.$$

We can use small slope approximations for the unit vector normal to the ice/snow surface $(-\partial\zeta/\partial x, -\partial\zeta/\partial y, 1)$ and take the dot product with the unit vector pointing to the sun $(\cos\phi_{\text{Sun}}\sin\theta_{\text{Sun}}, \sin\phi_{\text{Sun}}\sin\theta_{\text{Sun}}, \cos\theta_{\text{Sun}})$.

From the definition of θ_l we have

$$\cos\theta_l = \cos\theta_{\text{Sun}} - \sin\theta_{\text{Sun}} (\cos\phi_{\text{Sun}}\partial\zeta/\partial x + \sin\phi_{\text{Sun}}\partial\zeta/\partial y) \quad (2)$$

which oscillates around the value $\cos\theta_{\text{Sun}}$. As a result, the TOA reflectance given in the image oscillates around the value ρ_{true}. In general the variance of the normalized oscillations $<\cos^2\theta_l>/\cos^2\theta_{\text{Sun}} - 1$ can be decomposed into a modulation spectrum $E_m(k_x, k_y)$. This modulation spectrum is related to the surface elevation power spectral density $E(k_x, k_y)$, usually called "wave spectrum,"

$$E_m(k_x, k_y) = M^2 E(k_x, k_y) + N(k_x, k_y) \quad (3)$$

where $N(k_x, k_y)$ is a non-wave contribution to the image and the modulation transfer function M is given by

$$M = k \tan\theta_{\text{Sun}} \cos(\phi_{\text{Sun}} - \phi_w) \quad (4)$$

where ϕ_w is the wave propagation azimuth and the wavenumber vector is $(k_x = k\cos\phi_w, k_y = k\sin\phi_w)$. If there are no waves propagating in the azimuth perpendicular to that of the Sun, we may invert this relationship to estimate the wave spectrum $E(k_x, k_y)$, and from it the significant wave height,

$$H_s = 4\sqrt{\iint E(k_x, k_y)\, k\mathrm{d}k\mathrm{d}\phi_w}$$

In practice, the main difficulty is to separate the wave-induced changes in apparent reflectivity from heterogeneities in the image caused by water-ice contrasts at the edges of ice floes, variations in ice roughness, or different ice thicknesses.

In the example shown in Figure 6, we have chosen a 4 km by 4 km region of relatively uniform brightness (without large leads, clouds, or changes in ice reflectance). Filtering scales smaller than 100 m makes it easier to separate the swell spectral peak (dashed box) from other features. Assuming that the filtering did not significantly reduce the variance of our wave signal, we integrate the wave spectrum over the dashed box region. For this range of wave numbers the root mean square variation in $\rho_{\text{L1c}}/\rho_{\text{true}}$ is 0.009. Using the transfer function and integrating the surface elevation variance gives a significant wave height of 0.35 m (0.40 m when the image is filtered at 50 m), that is of the order of the values expected at 11 UTC at the location of Figure 5, with a strong reduction compared to the 4 UTC values, due to the general propagation of the swells toward the East. The wave field can be followed at least 200 km into the ice with an estimated significant wave height decreasing to 0.2 m (Figure 7).

Given the 1 s time difference between the acquisition of the B02 and B04 bands (Kudryavtsev et al., 2017), we can use the wave phase difference between the two bands to remove the 180° ambiguity on wave propagation,

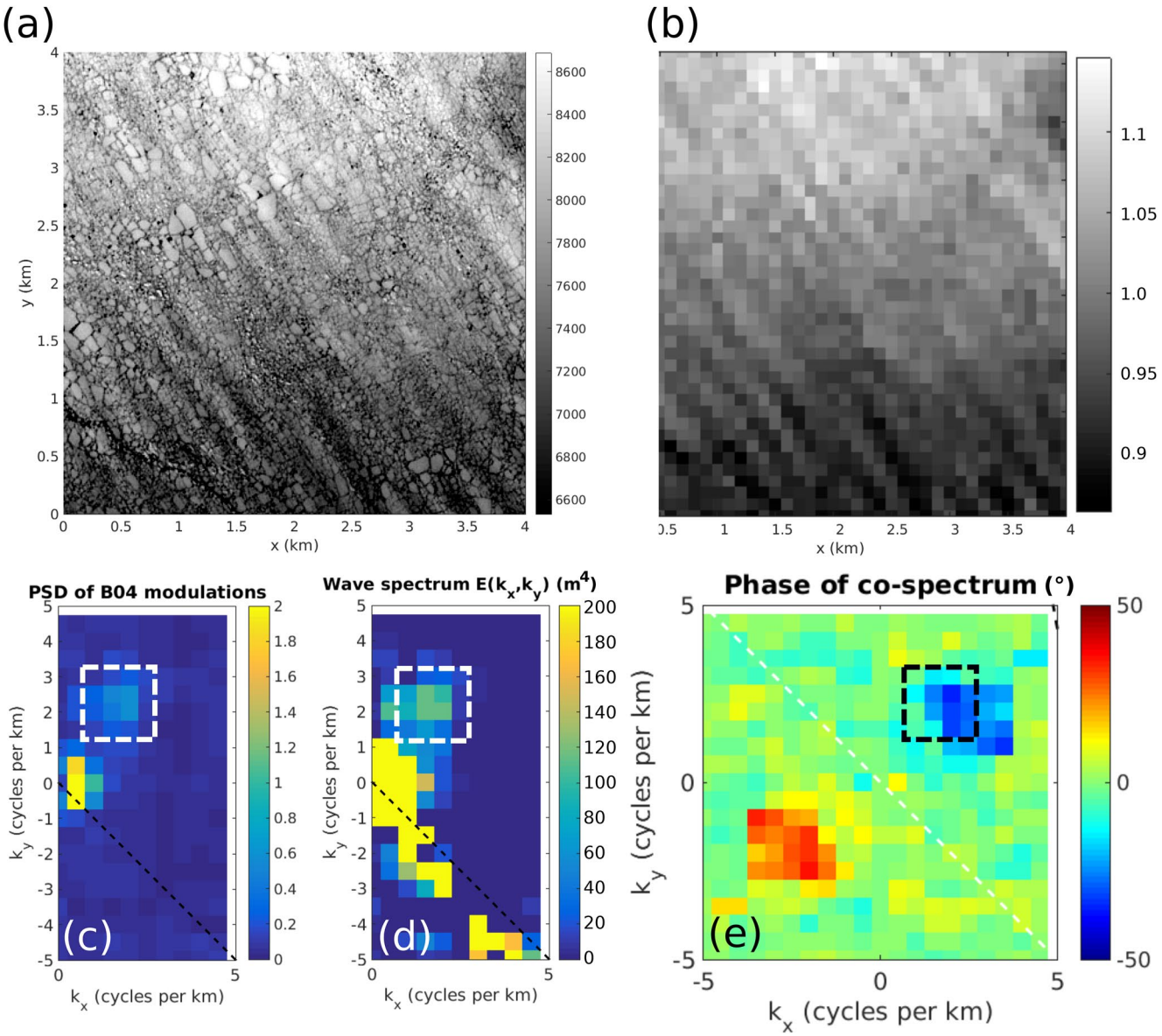

Figure 6. Processing of S2 B04 and B02 bands to obtain a wave spectrum. (a) Original image (b) subsampled image, normalized by the median image value (c) double-sided Power Spectral Density E_m of image modulation (d) single-sided Wave spectrum (e) phase of the co-spectrum of B04 and B02 images. The dashed box in panels (c–e) corresponds to the "wave partition" region of the spectral space where we expect wave signatures, and is the only place where the wave spectrum is expected to be correct. The non-wave contributions to the image $N(k_x, k_y)$ were estimated to be a constant equal to the median value of the modulation spectrum. The dashed line that goes through the origin is the blind azimuth, perpendicular to the sun azimuth for which waves produce no pattern in the image.

unless there are waves with similar energy levels propagating in opposite directions (Ardhuin et al., 2021). Further use of the wave phase to estimate surface currents is limited by the image sub-pixel co-registration accuracy (Yurovskaya et al., 2019), and the necessary averaging over a large area to reduce the phase noise. That phase noise would be lower for shorter wavelengths but these are not present in the ice.

3. Case of 12 March 2021

Instead of a local storm, we now look for off-ice winds and cloud-free conditions at the ice edge, in which case the waves are remotely generated swells. Also, after March 2019, spectra from CFOSAT's SWIM instrument are available (Hauser et al., 2017), providing measurements of wave spectra over open water. Finally we will also use Sentinel 3 data, in particular with FF-SAR processing that is capable of resolving wind-generated waves. Figure 8

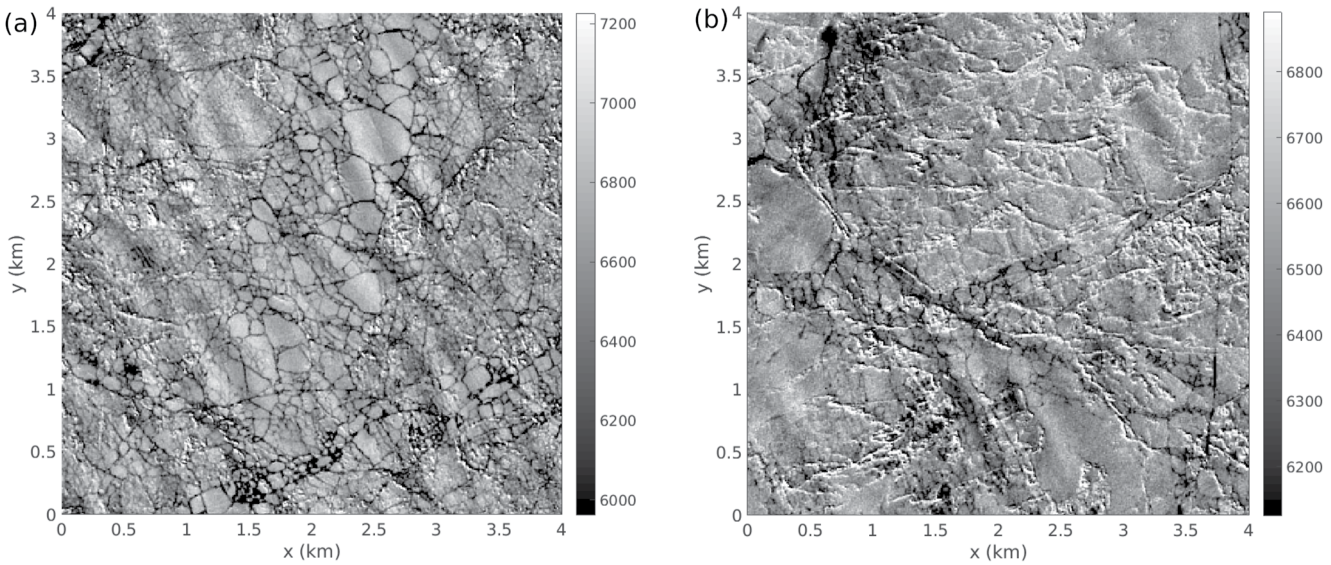

Figure 7. Other examples of wave patterns in sea ice at 11:07 UTC on 23 March 2019, (a) at 78.79°N, 50.12°E with an estimated wave height of 0.36 m (b) at 79.07°N, 50.80°E with an estimated wave height of 0.20 m.

shows a mosaic of Sentinel 2 imagery acquired around Svalbard at 11:08 UTC on 12 March 2021, and an example of colocated swell signatures in Sentinel 3 SRAL and Sentinel 2 MSI imagery.

Swells arrived in the region from a strong mid-Atlantic storm that peaked on 10 March with wave heights exceeding 14 m, and propagated to the Barents Sea through the gap between Iceland and the Faroe islands. These long swells with amplitudes around 1 m were superimposed on a local wind sea generated by a strong north-easterly wind system that expanded from the central Arctic into the Barents sea on 11 and 12 March. These winds led to a shift of the ice edge toward the south.

The ice cover East of Svalbard is characterized by a relatively straight East-West ice edge around 35°E and a bulging ice tongue around 20°E that often extends to Bear Island to the south (Figure 8a). This ice tongue was stretched to the south-west by the wind, which blew most of the clouds away and made it possible to see the ice. This ice tongue happens to be under a Sentinel 3B track that coincided within 10 min of the Sentinel two imagery. The more compact ice around 35°E was sampled later in the day by both Sentinel 3A (at 16:50) ICESat-2 at 18:14 and two CFOSAT passes at 6:50 and 14:40.

Observing waves close to the ice edge is challenging for all sensors. Optical imagery is obviously affected by clouds. The few bands of clouds and their shadows that are present over the ice tongue, around 75.5°N, 20°E, make it difficult to apply the technique presented in the previous section. Using a relatively homogenous piece of ice ($9 < x < 12$ km and $1 < y < 4$ km in Figure 8c) gives a wave height of about 0.44 m and a peak wavelength of 250 m. Heterogeneities in the optical image also include leads that are more numerous near the ice edge in the case of off-ice winds.

3.1. Wave Patterns in Sentinel-3 FF-SAR Imagery

Standard altimeter measurements, that provide significant wave heights in ice-free regions as the only sea state parameter, give a very limited picture of the complex sea state with swells and an opposing wind sea. Here, we show the first fully focused SAR (FF-SAR) processing of altimeter data in wave-impacted sea ice (Figure 8b). Level 1a data from Sentinel-3B are FF-SAR processed using the Delft Altimeter Toolbox (Kleinherenbrink et al., 2020). A Gaussian filter is applied in the along-track direction after which the waveforms are subsampled at 22 m along-track to ensure a better spectral response than standard multilooking approach. The waveforms are retracked using a threshold. Any drifts and jumps in the range are compensated for to align the leading edge of the waveforms, to ensure proper cross-track projection of the waveform bins. Then a normalization procedure is applied comparable to Altiparmaki et al. (2022) to compute the SAR contrast that is, the ratio

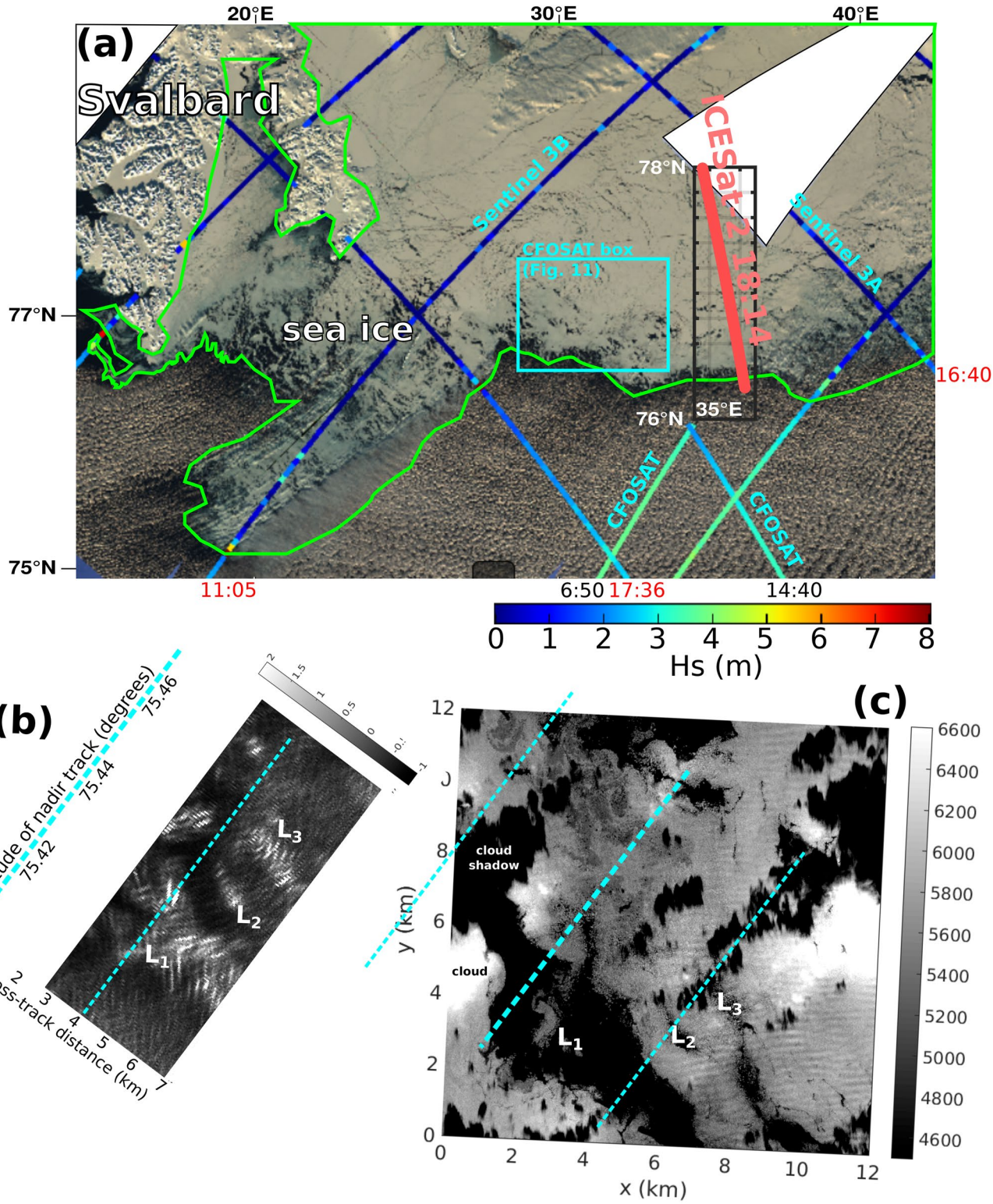

Figure 8.

of the high-resolution backscatter variations with respect to the low-resolution backscatter variations. For the low-resolution backscatter variations σ_{lpf}, we apply a two-dimensional Gaussian filter, which should filter the swell signals, but should capture the quickly changing backscatter from leads and sea ice. The normalized backscatter is then given as

$$\sigma_{\text{N}}(n,m) = \frac{\sigma(n,m) - \sigma_{\text{lpf}}(n,m)}{\sigma_{\text{lpf}}(n,m)}, \tag{5}$$

where $\sigma(n, m)$ is the backscatter in the waveform tail at bin n and along-track waveform m. Finally, the waveform bins are projected on the ground as a function of cross-track distance x using the relation

$$x(n) = \sqrt{(H + (n - n_{\text{ref}})\,\Delta r)^2 - H^2}, \tag{6}$$

where $n - n_{\text{ref}}$ is the relative waveform bin from the leading edge, Δr is the altimeter sampling distance, and H is the platform altitude.

As in ice-free conditions, swells give four peaks in the wave spectrum due to the left-right ambiguity of the measurement geometry and the similar signature of waves propagating in opposite directions. The bright regions marked "L1," "L2," and "L3" are different leads, regions of flat water or ice, that appear very bright in the radar image and dark in the optical image. Although Figure 8c was strongly saturated to show the wave patterns, leads are brighter and clearly distinct from cloud shadows. We note that the vertical wave patterns in both L1 and L3 are brighter than the horizontal wave pattern. The vertical bright stripes are actually east-west wave crests and trough patterns that are on the right hand side of the track and, given the measurement geometry that cannot distinguish left and right, are folded on the left hand side of our Figure 8b. However, we may use the knowledge of the swell direction to unfold the image, as done in Figure 9, now putting the stronger contrast of leads L1 and L3 on the right side of the track.

Just like in the case of ice-free water, the pattern in the FF-SAR is expected to come from a combination of velocity-bunching that is common to all SAR images (Ardhuin et al., 2015; Lyzenga et al., 1985), and range-bunching that is specific to near-nadir radar measurements (Peral et al., 2015). Given the general low slope of swell waves in sea ice, the nonlinear contributions to bunching are relatively weak and it may be possible to retrieve a wave spectrum from the image spectrum. However, the strong changes in backscattered radar power associated with leads create heterogeneities in the image that are similar to those in usual SAR imagery.

3.2. Wave Patterns in CFOSAT SWIM Data

The SWIM instrument is a wave spectrometer that measures the backscatter power as a function of range, with high resolution in range and averaging over 18 km in the perpendicular direction (Hauser et al., 2017, 2021). These measurements are made with beams that rotate in azimuth while keeping a fixed incidence angle. Here, we use data from the beam centered on the incidence angle of 6°. Due to the large-scale averaging across the beam, only the features that are exactly perpendicular to the azimuth contribute to the measured signal (Jackson et al., 1985). This is the principle of the wave spectrometer that is capable of resolving waves in their perpendicular direction thanks to a high resolution in range, and selecting only one wave direction (with 180° ambiguity) thanks to the very large-scale averaging in the perpendicular direction.

Over the oceans, the modulations in radar backscatter have been shown to correspond to waves, and the wave directional spectrum can be retrieved by combining wavenumber spectra obtained for different azimuths (Hauser et al., 2021; Le Merle et al., 2021). Over sea ice, the backscatter variation as a function of incidence angle and local ice slope is a priori very different, and also the backscatter can vary due to variations in ice properties and

Figure 8. Wave signatures in Sentinel-2, Sentinel-3B, and ICESat-2 on 12 March 2021. (a) The portion of ICESat-2 track where wave signals are detected in the Level3a ATL07 ice elevation product is show in pink, overlaid on the mosaic of Sentinel 2 imagery. Svalbard is to the left. The ice edge is the green line. Wave heights from nadir altimeters on CFOSAT, Sentinel 3A, and Sentinel 3B are shown in colors, with the time of the tracks indicated on the edge of the image. (b) Fully focused Sentinel 3B waveforms showing the signature of leads (bright regions, three of them are marked L_1, L_2, and L_3). Swell patterns with wavelengths around 250 m are visible in both leads and sea ice, with 2 main orientations due to the left-right ambiguity in the cross-track direction. (c) Sentinel-2 B04 image showing leads, clouds, and cloud shadows, and a clear swell signature with a 250 m wavelength. In (b and c), the nadir ground track of Sentinel 3B is shown with the thick dashed cyan line, and the thinner lines indicate the location of pixels 4 km from nadir, on both sides of the track, corresponding the lines.

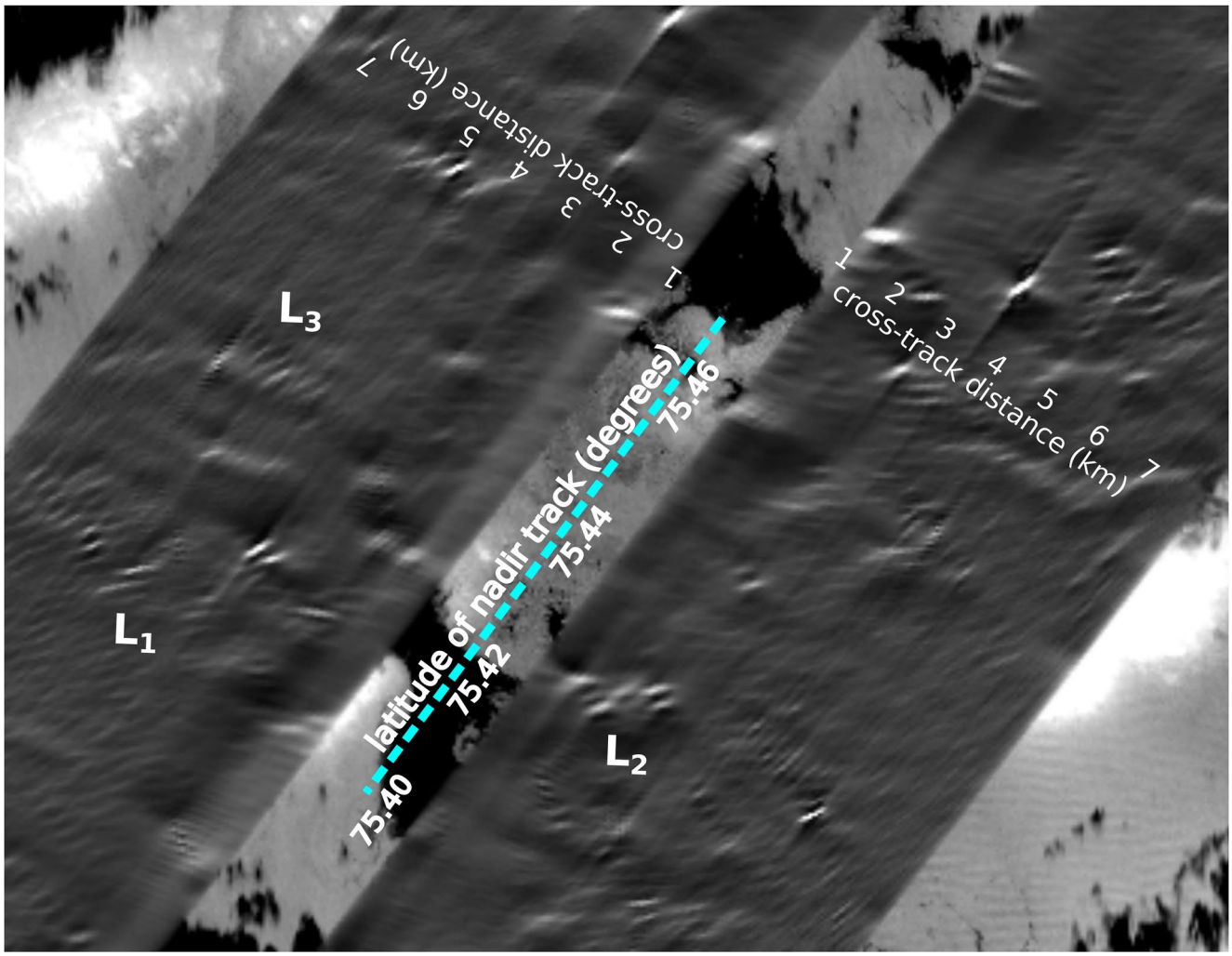

Figure 9. Unfolded Sentinel-3 radar backscatter from Full-Focus SAR (FF-SAR) processing using Fourier analysis to separate near-horizontal features from near-vertical features in Figure 8b, and inverse Fourier transform that generates a left-side image with near-horizontal features and a right-side image with what was near-vertical when folded to the left which now appears also near-horizontal. The background image is Sentinel-2.

the presence of leads. The analysis presented here is, to the best of our knowledge, the first attempt at interpreting SWIM radar modulations over sea ice.

CFOSAT SWIM data used are the L2S products V1.0 from IWWOC processing center at Ifremer. The fluctuation spectra are estimated after mean speckle noise removal and non-wave signature low wavenumber filter. Additional filtering is used over sea ice by looking at the variability of spectral coefficients estimated on successive 2.56 km segments within the 18 km diameter footprint. Spectral coefficients for which the standard deviation exceed two times the mean value over all segments are discarded.

Figure 10a shows a 7 km by 8 km piece of Sentinel-2 image around 76.7°N, 30°E with a dominant wave propagation direction around 37° clockwise from North. Figure 10b shows a wider area from the same image, now also including the 1D spectra from SWIM shown as an overlaid color strip with warmer colors corresponding to higher power spectral density, and each strip occupies the same length as the ground ranges of the SWIM footprint (note that the footprint also covers the same distance in the perpendicular direction). To facilitate the interpretation, the strip that is in the magenta box, with an azimuth 37° clockwise from North, is plotted in Figure 10c with a more usual power spectral density as a function of wavenumbers. The overlaid spectra from the Sentinel-2 and Sentinel-1 images have a similar shape with a peak wavenumber around 0.022 rad/m. Although not exactly colocated in time and space, the ICESat-2 data also shares similar wavelengths when assuming that the wave

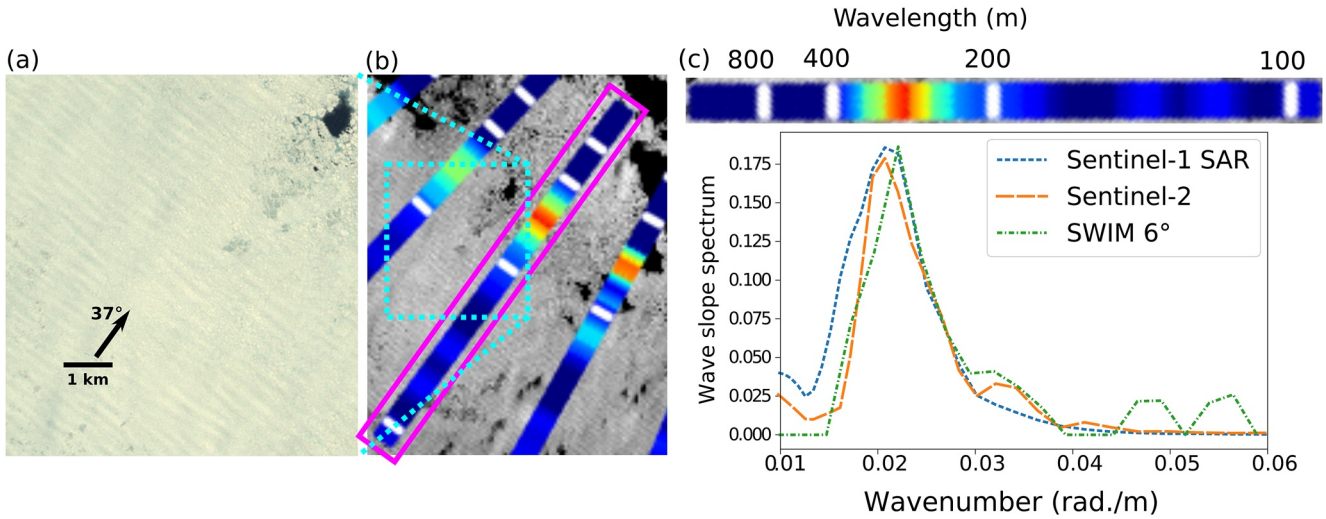

Figure 10. (a) and (b) Wave patterns around 76.7°N, 30°E on 12 March 2021, and CFOSAT-SWIM spectrum in azimuth 37° using the 6° incidence beam, compared to the spectra of Sentinel-1 and Sentinel-2 images in the same region. In (b) SWIM modulation spectra from the 6° incidence beam are overlaid as colored strips. The white marks in the colored strip correspond to wavelengths 800, 400, 200, and 100 m. (c) SWIM spectrum for the azimuth 37° clockwise from North in strip form as a the usual power spectral density as a function of wavenumber, compared with spectra in the same direction from Sentinel-1 and Sentinel-2 imagery. ICESat-2 data was averaged from the three strong beams over the latitude range 77.75°–77.9° using Fourier transforms over 0.05° in latitude. The wavenumber was multiplied by the proper projection from the satellite track to the 37° azimuth, common to the other data sets.

propagation azimuth is 37°. The higher energy at high wavenumbers in ICESat-2 is probably induced by noise, and it is much more pronounced for the weak beams (not shown).

Looking at SWIM spectra for all directions shows that SWIM detects peaks at the expected wavelengths and directions of the swell (Figure 11). However, peaks in the modulation spectrum are also present at a wide range of scales for directions perpendicular to the wave propagation. These peaks that cannot be associated with waves are highlighted with magenta arrows. The background Sentinel-2 image suggests that the regions where non-wave signatures are present are the regions where leads have scales that overlap with the usual range of wavelengths. In that case it is impossible to separate radar backscatter variations coming from a patchy ice cover with the modulation caused by waves.

4. Discussion and Conclusion

Wave patterns in Arctic sea ice have been found in all radar and optical measurements near the ice edge. These observations can provide useful observation for understanding the interactions of waves and sea ice. Previous works have insisted on the variability of wave attenuation and more measurements of wave attenuation are needed to better understand the processes at play. In this context, the frequent detection of waves in sea ice in ICESat-2 data (Horvat et al., 2020) can provide a very useful data set for waves in Arctic sea ice, allowing for a quantitative measurement of wave height, wavelength and direction, and the attenuation of waves along the altimeter track. Because the altimeter track does not often coincide with the wave direction the data may require some ancillary numerical modeling for its interpretation: the apparent reduction in wave height may be caused by open water gradients in the wave field and not by ice-induced effects.

The less frequent appearance of wave patterns in Sentinel-2 imagery, which requires a near-grazing sun illumination in addition to the absence of clouds, provides further information. In particular the size of floes can be estimated, at least qualitatively, which is key to interpret the wave attenuation. Also, having a two-dimensional image may help in resolving gradients in sea state long the ice edge that should contain both different attenuation histories and a signature of waves-current interactions near the ice edge (von Appen et al., 2018). Difficulties in the interpretation of wave signature in optical imagery will remain due to the presence of clouds and the heterogeneities in the ice cover.

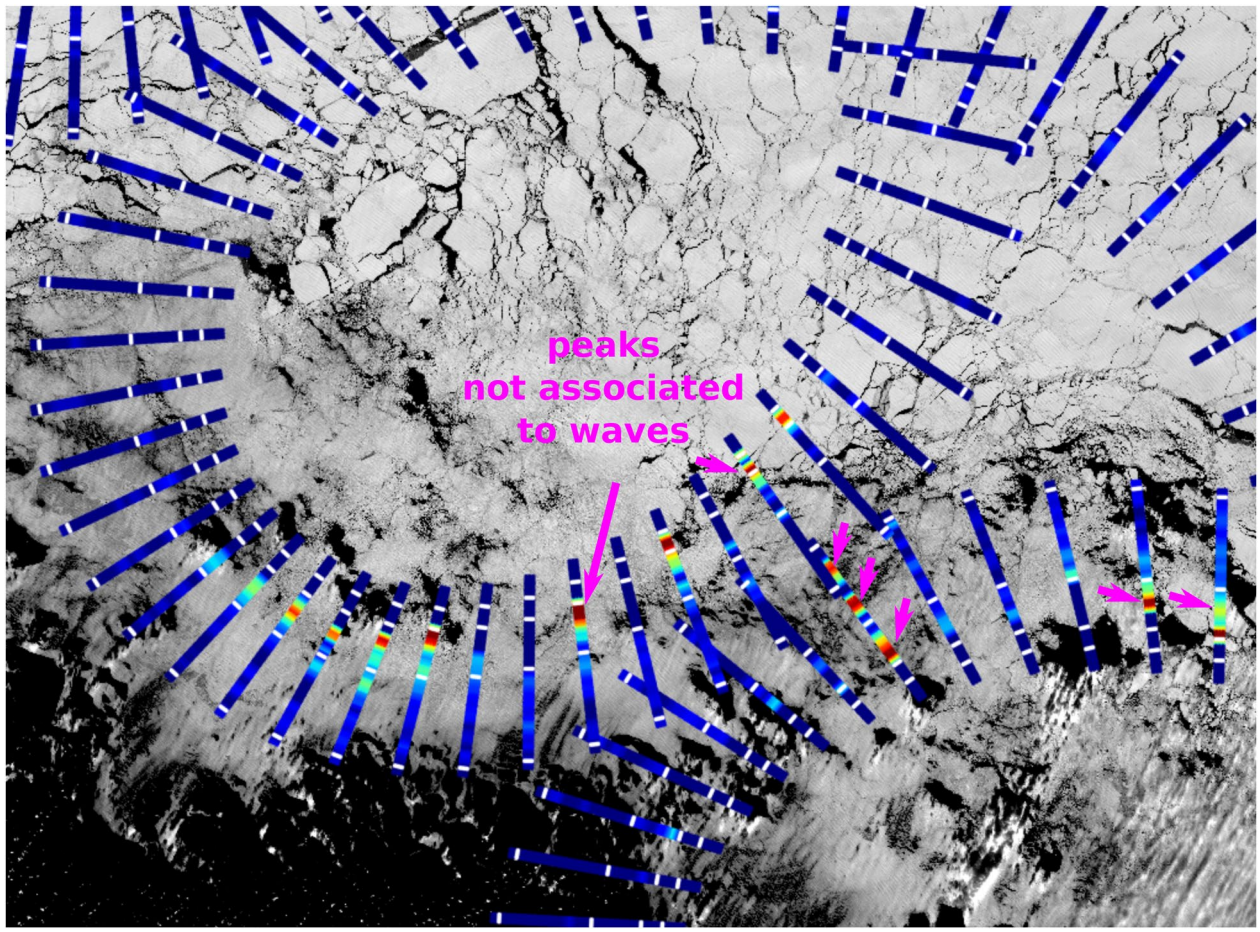

Figure 11. Same as Figure 10b, but over a wider area, corresponding to the cyan box in Figure 8.

Finally, wave-resolving radar data over sea ice are more readily obtained but their quantitative analysis is not so straightforward (Ardhuin et al., 2017). The novel capability provided by FF-SAR processing is clearly an interesting source of data that can be obtained from recent altimeter missions (Cryosat-2, Sentinel-3, and Sentinel-6-Michael-Freilich), as well as planned missions, including the dual frequency altimeter Cristal.

We have presented observations of wave patterns in sea ice using three types of satellite radars, Sentinel-1 SAR imagery, Sentinel-3 FF-SAR altimetry, and SWIM modulation spectra, and two types of optical observations, ICESat-2 lidar ice height measurements and Sentinel-2 imagery. Only the Sentinel-1 SAR has been previously validated in detail (Ardhuin et al., 2017) and used for science applications (Ardhuin et al., 2018; Stopa, Ardhuin, et al., 2018). Here, we have expanded on the previous detection of waves in ice by Horvat et al. (2020) to show that a quantitative analysis of wave heights, directions, and wavelengths was possible from ICESat-2 data. We have also exhibited and interpreted wave signatures in Sentinel-2, Sentinel-3 FF-SAR, and SWIM data. The quantitative interpretation of the last two measurements will require further work in developing a forward model that represents range bunching, velocity bunching, and possibly other effects. Taken together, there is a great potential for a synergistic use of these 5 data sources, some of which allow exact colocation in space with time differences of only a few minutes. Building colocated data sets of waves in ice observations can certainly help to reach a more quantitative understanding of the radar measurements, leading to science applications on the understanding of wave-ice interactions as well as practical applications to marine safety and Earth System modeling.

Data Availability Statement

ICESat-2 data was obtained from NASA National Snow and Ice Data Center Distributed Active Archive Center, Boulder, Colorado, https://doi.org/10.5067/ATLAS/ATL07.005, and CFOSAT modulation spectra data was obtained from Ifremer at https://data-cersat.ifremer.fr/projects/iwwoc/.

Acknowledgments
We acknowledge the use of Copernicus Sentinel 1, 2, and 3 data, obtained from the Copernicus Science Hub https://scihub.copernicus.eu. F.C. was supported by ESA through the ARKTALAS contract AO/1-9595/18/NL/LF. We thank Bertrand Chapron for fruitful discussions.

References

Altiparmaki, O., Kleinherenbrink, M., Naeije, M., Slobbe, C., & Visser, P. (2022). Sar altimetry data as a new source for swell monitoring. *Geophysical Research Letters*, *49*(7), e2021GL096224. https://doi.org/10.1029/2021GL096224

Ardhuin, F., Alday, M., & Yurovskaya, M. (2021). Total surface current vector and shear from a sequence of satellite images: Effect of waves in opposite directions. *Journal of Geophysical Research: Oceans*, *126*(7), e2021JC017342. https://doi.org/10.1029/2021JC017342

Ardhuin, F., Boutin, G., Stopa, J., Girard-Ardhuin, F., Melsheimer, C., Thomson, J., et al. (2018). Wave attenuation through an Arctic marginal ice zone on 12 october, 2015: 2: Numerical modeling of waves and associated ice break-up. *Journal of Geophysical Research: Oceans*, *123*(8), 5652–5668. https://doi.org/10.1002/2018JC013784

Ardhuin, F., Chapron, B., Collard, F., Smith, M., Stopa, J., Thomson, J., et al. (2017). Measuring ocean waves in sea ice using SAR imagery: A quasi-deterministic approach evaluated with sentinel-1 and in situ data. *Remote Sensing of Environment*, *189*, 211–222. https://doi.org/10.1016/j.rse.2016.11.024

Ardhuin, F., Collard, F., Chapron, B., Girard-Ardhuin, F., Guitton, G., Mouche, A., & Stopa, J. (2015). Estimates of ocean wave heights and attenuation in sea ice using the sar wave mode on Sentinel-1A. *Geophysical Research Letters*, *42*(7), 2317–2325. https://doi.org/10.1002/2014GL062940

Ardhuin, F., Otero, M., Merrifield, S., Grouazel, A., & Terrill, E. (2020). Ice breakup controls dissipation of wind waves across southern ocean sea ice. *Geophysical Research Letters*, *47*(13), e2020GL087699. https://doi.org/10.1029/2020GL087699

Ardhuin, F., Sutherland, P., Doble, M., & Wadhams, P. (2016). Ocean waves across the Arctic: Attenuation due to dissipation dominates over scattering for periods longer than 19 s. *Geophysical Research Letters*, *43*(11), 5775–5783. https://doi.org/10.1002/2016GL068204

Boutin, G., Ardhuin, F., Dumont, D., Sévigny, C., Girard-Ardhuin, F., & Accensi, M. (2018). Floe size effects on wave-ice interactions: Theoretical background, implementation and applications. *Journal of Geophysical Research: Oceans*, *123*(7), 4779–4805. https://doi.org/10.1029/2017JC013622

Collins, C., Rogers, W. E., Marchenko, A., & Babanin, A. V. (2015). In situ measurements of an energetic wave event in the Arctic marginal ice zone. *Geophysical Research Letters*, *42*(6), 1863–1870. https://doi.org/10.1002/2015GL063063

Dirmhirn, I., & Eaton, F. D. (1975). Some characteristics of the albedo of snow. *Journal of Applied Mechanics*, *14*(3), 375–379. https://doi.org/10.1175/1520-0450(1975)014<0375:SCOTAO>2.0.CO;2

Doble, M. J., Skourup, H., Wadhams, P., & Geiger, C. A. (2011). The relation between Arctic sea ice surface elevation and draft: A case study using coincident AUV sonar and airborne scanning laser. *Journal of Geophysical Research*, *116*, COOE03. https://doi.org/10.1029/2011JC007076

Hasselmann, K., Chapron, B., Aouf, L., Ardhuin, F., Collard, F., Engen, G., et al. (2012). The ERS SAR wave mode: A breakthrough in global ocean wave observations. In *Ers missions: 20 years of observing earth* (pp. 165–198). European Space Agency.

Hauser, D., Tison, C., Amiot, T., Delaye, L., Corcoral, N., & Castillan, P. (2017). SWIM: The first spaceborne wave scatterometer. *IEEE Transactions on Geoscience and Remote Sensing*, *55*(5), 3000–3014. https://doi.org/10.1109/tgrs.2017.2658672

Hauser, D., Tourain, C., Hermozo, L., Alraddawi, D., Aouf, L., Chapron, B., et al. (2021). New observations from the SWIM radar on-board CFOSAT: Instrument validation and ocean wave measurement assessment. *IEEE Transactions on Geoscience and Remote Sensing*, *59*(1), 5–26. https://doi.org/10.1109/tgrs.2020.2994372

Horvat, C., Blanchard-Wrigglesworth, E., & Petty, A. (2020). Observing waves in sea ice with ICESat-2. *Geophysical Research Letters*, *47*(10), e2020GL087629. https://doi.org/10.1029/2020GL087629

Horvat, C., & Tziperman, E. (2017). The evolution of scaling laws in the sea ice floe size distribution. *Journal of Geophysical Research: Oceans*, *122*(9), 7630–7650. https://doi.org/10.1002/2016jc012573

Jackson, F. C., Walton, W. T., & Baker, P. L. (1985). Aircraft and satellite measurement of ocean wave directional spectra using scanning-beam microwave radars. *Journal of Geophysical Research*, *90*(C1), 987–1004. https://doi.org/10.1029/jc090ic01p00987

Kaleschke, L., Tian-Kunze, X., Maaß, N., Mäkynen, M., & Drusch, M. (2012). Sea ice thickness retrieval from SMOS brightness temperatures during the arctic freeze-up period. *Geophysical Research Letters*, *39*(5), L05501. https://doi.org/10.1029/2012gl050916

Kleinherenbrink, M., Naeije, M., Slobbe, C., Egido, A., & Smith, W. (2020). Observations of polar ice fields. *Remote Sensing of Environment*, *237*, 111589. https://doi.org/10.1016/j.rse.2019.111589

Kudryavtsev, V., Yurovskaya, M., Chapron, B., Collard, F., & Donlon, C. (2017). Sun glitter imagery of surface waves. part 1: Directional spectrum retrieval and validation. *Journal of Geophysical Research: Oceans*, *122*(2), 1369–1383. https://doi.org/10.1002/2016JC012425

Kwok, R., Petty, A. A., Cunningham, G., Markus, T., Hancock, D., Ivanoff, A., et al. (2021). *Atlas/icesat-2 l3a sea ice height, version 5*. Tech. Rep. No. 2007/5. NASA National Snow and Ice Data Center Distributed Active Archive Center. https://doi.org/10.5067/ATLAS/ATL07.005

Le Merle, E., Hauser, D., Peureux, C., Aouf, L., Schippers, P., Dufour, C., & Dalphinet, A. (2021). Directional and frequency spread of surface ocean waves from swim measurements. *Journal of Geophysical Research: Oceans*, *126*(7), e2021JC017220. https://doi.org/10.1029/2021JC017220

Lyzenga, D. R., Shuchman, R. A., Lyden, J. D., & Rufenach, C. L. (1985). SAR imaging of waves in water and ice: Evidence for velocity bunching. *Journal of Geophysical Research*, *90*(C1), 1031–1036. https://doi.org/10.1029/jc090ic01p01031

Peral, E., Rodriguez, E., & Esteban-Fernandez, D. (2015). Impact of surface waves on SWOT's projected ocean accuracy. *Remote Sensing*, *7*(11), 14509–14529. https://doi.org/10.3390/rs71114509

Rogers, W. E., Thomson, J., Shen, H. H., Doble, M. J., Wadhams, P., & Cheng, S. (2016). Dissipation of wind waves by pancake and frazil ice in the autumn beaufort sea. *Journal of Geophysical Research*, *121*(11), 7991–8007. https://doi.org/10.1002/2016JC012251

Squire, V. A. (2020). Ocean wave interactions with sea ice: A reappraisal. *Annual Review of Fluid Mechanics*, *52*(1), 37–60. https://doi.org/10.1146/annurev-fluid-010719-060301

Stopa, J. E., Ardhuin, F., & Girard-Ardhuin, F. (2016). Wave climate in the Arctic 1992-2014: Seasonality and trends. *The Cryosphere*, *10*(4), 1605–1629. https://doi.org/10.5194/tc-10-1605-2016

Stopa, J. E., Ardhuin, F., Thomson, J., Smith, M. M., Kohout, A., Doble, M., & Wadhams, P. (2018). Wave attenuation through an arctic marginal ice zone on 12 october, 2015: 1. Measurement of wave spectra and ice features from sentinel 1A. *Journal of Geophysical Research: Oceans*, *123*(5), 3619–3634. https://doi.org/10.1029/2018JC013791

Stopa, J. E., Sutherland, P., & Ardhuin, F. (2018). Strong and highly variable push of ocean waves on southern ocean sea ice. *Proceedings of the National Academy of Sciences*, *115*(23), 5861–5865. https://doi.org/10.1073/pnas.1802011115

Sutherland, P., & Dumont, D. (2018). Marginal ice zone thickness and extent due to wave radiation stress. *Journal of Physical Oceanography*, *48*(8), 1885–1901. https://doi.org/10.1175/JPO-D-17-0167.1

Sutherland, P., & Gascard, J. C. (2016). Airborne remote sensing of ocean wave directional wavenumber spectra in the marginal ice zone. *Geophysical Research Letters*, *43*(10), 4659–4664. https://doi.org/10.1002/grl.53444

The WAVEWATCH III® Development Group. (2019). *User manual and system documentation of WAVEWATCH III® version 6.07 (Tech. Note No. 333)*. (p. 465 + Appendices). NOAA/NWS/NCEP/MMAB.

Thomson, J., Ackley, S., Girard-Ardhuin, F., Ardhuin, F., Babanin, A., Boutin, G., et al. (2018). Overview of the arctic sea state and boundary layer physics program. *Journal of Geophysical Research: Oceans*, *123*(12), 8674–8687. https://doi.org/10.1002/2018JC013766

Thomson, J., Hoseková, L., Meylan, M. H., Kohout, A. L., & Kumar, N. (2021). Spurious rollover of wave attenuation rates in sea ice caused by noise in field measurements. *Journal of Geophysical Research: Oceans*, *47*(3), e2020JC016606. https://doi.org/10.1029/2020JC016606

Thomson, J., Lund, B., Hargrove, J., Smith, M. M., Horstmann, J., & MacKinnon, J. A. (2021). Wave-driven flow along a compact marginal ice zone. *Geophysical Research Letters*, *48*(3), e2020GL090735. https://doi.org/10.1029/2020GL090735

Thomson, J., & Rogers, W. E. (2014). Swell and sea in the emerging Arctic Ocean. *Geophysical Research Letters*, *41*(9), 3136–3140. https://doi.org/10.1002/2014GL059983

von Appen, W.-J., Wekerle, C., Hehemann, L., Schourup-Kristensen, V., Konrad, C., & Iversen, M. H. (2018). Observations of a subme-soscale cyclonic filament in themarginal ice zone. *Geophysical Research Letters*, *45*, 6141–6149. https://doi.org/10.1029/2018GL077897

Wadhams, P., Squire, V. A., Ewing, J. A., & Pascal, R. W. (1986). The effect of the marginal ice zone on the directional wave spectrum of the ocean. *Journal of Physical Oceanography*, *16*(2), 358–376. https://doi.org/10.1175/1520-0485(1986)016<0358:teotmi>2.0.co;2

Yu, Y., Sandwell, D. T., Gille, S. T., & Boas, A. B. V. (2021). Assessment of ICESat-2 for the recovery of ocean topography. *Geophysical Journal International*, *226*(1), 456–467. https://doi.org/10.1093/gji/ggab084

Yurovskaya, M., Kudryavtsev, V., Chapron, B., & Collard, F. (2019). Ocean surface current retrieval from space: The sentinel-2 multispectral capabilities. *Remote Sensing of Environment*, *234*, 111468. https://doi.org/10.1016/j.rse.2019.111468